Received: 8 May 2018 | Revised: 17 July 2018 | Accepted: 19 July 2018

DOI: 10.1002/mrm.27491

FULL PAPER

Magnetic Resonance in Medicine

On the accuracy and precision of PLANET for multiparametric MRI using phase-cycled bSSFP imaging

Yulia Shcherbakova[1] | **Cornelis A. T. van den Berg**[2] | **Chrit T. W. Moonen**[1] | **Lambertus W. Bartels**[1]

[1]Center for Image Sciences, Imaging Division, University Medical Center Utrecht, Utrecht, the Netherlands

[2]Department of Radiotherapy, Imaging Division, University Medical Center Utrecht, Utrecht, the Netherlands

Correspondence
Yulia Shcherbakova, Center for Image Sciences, Imaging Division, University Medical Center Utrecht, Heidelberglaan 100, Room Q.03.4.21, 3508 GA Utrecht, the Netherlands.
Email: Y.Shcherbakova@umcutrecht.nl

Funding information
The Netherlands Organisation for Scientific Research (NWO), Domain Applied and Engineering Sciences, Grant/Award Number: grant 12813

Purpose: In this work we demonstrate how sequence parameter settings influence the accuracy and precision in T_1, T_2, and off-resonance maps obtained with the PLANET method for a single-component signal model. In addition, the performance of the method for the particular case of a two-component relaxation model for white matter tissue was assessed.

Methods: Numerical simulations were performed to investigate the influence of sequence parameter settings on the accuracy and precision in the estimated parameters for a single-component model, as well as for a two-component white matter model. Phantom and in vivo experiments were performed for validation. In addition, the effects of Gibbs ringing were investigated.

Results: By making a proper choice for sequence parameter settings, accurate and precise parameter estimation can be achieved for a single-component signal model over a wide range of relaxation times at realistic SNR levels. Due to the presence of a second myelin-related signal component in white matter, an underestimation of approximately 30% in T_1 and T_2 was observed, predicted by simulations and confirmed by measurements. Gibbs ringing artifacts correction improved the precision and accuracy of the parameter estimates.

Conclusion: For a single-component signal model there is a broad "sweet spot" of sequence parameter combinations for which a high accuracy and precision in the parameter estimates is achieved over a wide range of relaxation times. For a multi-component signal model, the single-component PLANET reconstruction results in systematic errors in the parameter estimates as expected.

KEYWORDS
accuracy, phase-cycled bSSFP, precision, relaxometry, SNR

1 | INTRODUCTION

Measurements of longitudinal (T_1) and transverse (T_2) relaxation times are used widely in many different applications to assess physical and physiological characteristics of tissues[1] associated with a specific disease, and changes therein with disease progression or regression as a response to therapy. Another emerging application is synthetic MRI,[2,3] in which

images with various contrasts based on signal weighting are synthetically generated from T_1, T_2, and proton density maps.

Many quantitative MRI techniques exist, including many approaches for relaxometry and the recently introduced MR fingerprinting approach.[4] In addition to the standard time-consuming methods for T_1 and T_2 mapping, which are based on 2D inversion-recovery spin-echo and multi-echo spin-echo sequences, there are many fast SSFP-based imaging techniques.[5] Some of them rely on the inversion recovery method with multiple low flip angle (FA) excitation pulses, such as the Look-Locker method.[6] Some are based on the variable FA approach, such as DESPOT (driven equilibrium single-pulse observation of T_1 and T_2),[7-9] or on multiple-echo approaches, such as DESS (double-echo steady state) and TESS (triple-echo steady state).[10,11]

Balanced SSFP (bSSFP) sequences deserve special attention due to their rapid acquisition time and high SNR efficiency. Despite sensitivity to local off-resonance, bSSFP has been successfully used for quantitative relaxometry,[12-14] especially for simultaneous T_1 and T_2 quantification.[15,16]

We recently proposed a method named PLANET[17] to simultaneously map the relaxation parameters T_1 and T_2, to the local off-resonance Δf_0, the RF phase, and the banding free magnitude image using a phase-cycled bSSFP sequence. Linear least-squares fitting of an ellipse to the complex-valued bSSFP data acquired with an RF phase incrementing scheme is first applied. This is followed by quantitative parameter estimation through analytical expressions that were derived from the geometrical characteristics of the ellipse.[17] The method uses standard pulse sequences and can be easily performed on clinical MR scanners within an acceptable time. Additionally, the reconstruction time is very short due to the use of a linear least-squares fitting (approximately 6-7 seconds per slice of matrix size 224×224).

In this work, we investigated how sequence parameter settings, such as FA, TR, and number of RF phase increment steps influence the accuracy and precision of quantitative T_1, T_2, and Δf_0 estimation using the PLANET method.

The PLANET model is based on a Lorentzian single-component relaxation model, which results in a symmetric bSSFP magnitude profile. However, in the case of the presence of a second component with a different frequency distribution and different relaxation parameter values, the bSSFP profile becomes asymmetric, as was pointed out by Miller et al.[18]

To investigate this issue, we paid special attention to the particular case of white matter (WM) tissue in the human brain, where the bSSFP profile is known to be asymmetric[19] due to the presence of a second signal component related to myelin with relatively short relaxation times. Many studies have demonstrated the presence of multicomponent T_1 and T_2 in the brain,[20-32] many of them were reviewed by Alonso-Ortiz et al.[33] We performed numerical simulations for WM using a two-component model to assess the accuracy and precision in parameter estimates. In addition, we validated the results experimentally.

The impact and mitigation of Gibbs ringing on PLANET was studied more in depth, motivated by the realization that the RF phase-cycling spatially shifts the banding artifacts, causing the Gibbs ringing to be in principle different for each phase-cycled image. This may result in systematic errors in calculated T_1 and T_2 maps, especially when low spatial resolution data are acquired.

In we demonstrated the feasibility of quantitative parameter mapping at realistic SNRs using the PLANET method.[17] The results we present here demonstrate that improvement in the accuracy and precision of all quantitative parameter estimates can be obtained by making an optimal choice for the sequence parameter settings.

2 | METHODS

First, for a single-component signal model, we investigated how the precision and accuracy of the estimated relaxation times T_1 and T_2, the local off-resonance Δf_0, as well as the SNR depend on the sequence parameter settings. For this purpose, we performed numerical simulations to investigate how the choice of parameter settings for FA, TR, and number of cycles N influences the absolute and relative errors in the parameter estimates. To provide guidance in practical use of the PLANET method, we determined the minimum SNR required to achieve a certain precision in all estimated parameters, which we chose to be equal to 5% of the mean parameter values. The simulation framework we developed can easily be used to repeat such investigations using other criteria. To demonstrate the performance of the method at high and low SNR levels, experiments were performed using a calibrated phantom on a 1.5T MR scanner.

Second, we investigated the case of a two-component relaxation model, particularly WM tissue. Again, we performed Monte Carlo simulations to assess the accuracy and precision of the quantitative parameter estimates. To validate the simulation results of a two-component model, in vivo brain experiments were performed in healthy volunteers at 3T.

Third, we investigated the effects of Gibbs ringing on the performance of the PLANET method. Using numerical simulations, we assessed the accuracy and precision in parameter estimates dependent on the chosen acquisition voxel size, and the effects of using Gibbs ringing filtering. To demonstrate the extent of Gibbs ringing effects, experiments in a phantom and in vivo in the brain of a healthy volunteer were performed at 1.5T.

2.1 | Single-component phase-cycled bSSFP signal model

The complex phase-cycled bSSFP signal can be described as[34,35]

$$I = M_{\text{eff}} \cdot \frac{1 - ae^{i\theta}}{1 - bcos\theta} \cdot e^{i\varphi} \tag{1}$$

where

$$M_{\text{eff}} = e^{-\frac{TE}{T_2}} \frac{KM_0(1-E_1)\sin\alpha}{1-E_1\cos\alpha - E_2^2(E_1-\cos\alpha)}, \quad a = E_2, b = \frac{E_2(1-E_1)(1+\cos\alpha)}{1-E_1\cos\alpha - E_2^2(E_1-\cos\alpha)} \tag{2}$$

$$\varphi = 2\pi\left(\delta_{CS} + \Delta f_0\right) TE + \varphi_{RF}, \tag{3}$$

φ is the rotation angle of an ellipse around the origin regarding to its initial vertical form[34] at TE = 0, $E_1 = \exp(-\frac{TR}{T_1})$, $E_2 = \exp(-\frac{TR}{T_2})$, KM_0 is product of the thermal equilibrium magnetization M_0 and the magnitude of the combined receive field K, α is the flip angle, TR is the repetition time, θ is the resonance offset angle (in radians), $\theta = \theta_0 - \Delta\theta$, where $\theta_0 = 2\pi\left(\delta_{CS} + \Delta f_0\right) TR$, Δf_0 is the off-resonance (in Hz), δ_{CS} is the chemical shift of the species (in Hz) with respect to the water peak, $\Delta\theta$ is the user-controlled RF phase increment (in radians), and φ_{RF} is the RF phase offset, related to the combination of RF transmit and receive phases (in radians).

2.1.1 | Accuracy and precision

The accuracy of the method for a single-component model was assessed by calculating the relative error (ε) in T_1, T_2, and Δf_0 estimates:

$$\varepsilon_{T_1} = \frac{\bar{T}_1 - T_{1true}}{T_{1true}} \cdot 100\% \varepsilon_{T_2} = \frac{\bar{T}_2 - T_{2true}}{T_{2true}} \cdot 100\%,$$

$$\varepsilon_{\Delta f_0} = \frac{\Delta\bar{f}_0 - \Delta f_{0true}}{\Delta f_{0true}} \cdot 100\%. \tag{4}$$

The precision of the method was assessed by calculating the relative SD of T_1, T_2, and Δf_0 estimates as follows:

$$SD_{T_1} = \frac{\sqrt{\frac{1}{Z}\sum_{i=1}^{Z}\left(T_1^i - \bar{T}_1\right)^2}}{\bar{T}_1} \cdot 100\%, SD_{T_2} = \frac{\sqrt{\frac{1}{Z}\sum_{i=1}^{Z}\left(T_2^i - \bar{T}_2\right)^2}}{\bar{T}_2} \cdot 100\%,$$

and

$$SD_{\Delta f_0} = \frac{\sqrt{\frac{1}{Z}\sum_{i=1}^{Z}\left(\Delta f_0^i - \Delta\bar{f}_0\right)^2}}{\Delta\bar{f}_0} \cdot 100\%, \tag{5}$$

where $\bar{X} = \frac{1}{Z}\sum_{i=1}^{Z} X^i$ refers to the average of the simulated values X^i, assuming a true value of X_{true} (for parameters T_1, T_2, and Δf_0), and Z is the total number of simulations.

2.1.2 | Numerical simulations

To investigate how the precision and accuracy in all parameter estimates depend on choices for FA, TR, and N, Monte Carlo simulations were performed for FA in the range of 0º-90º, TR in the range of 0-50 ms, and number N of RF phase increment steps from 6 to 16 with increments $\Delta\theta_n = \frac{2\pi n}{N} - \pi$, $n = \{0, 1, .., N\text{-}1\}$, and the initial parameter settings $KM_0 = 10\,000$, $\Delta f_0 = 10$ Hz, single peak with $\delta_{CS} = 0$, and $\varphi_{RF} = 0$. The chosen Δf_0 corresponds to the average off-resonance observed experimentally in the brain at 3T in the center of the FOV, and the chosen combination of $T_1 = 830$ ms and $T_2 = 80$ ms represents WM at 3T.[36] Gaussian noise was added independently to the real and imaginary data, resulting in an SNR ranging from 30 to 150 for WM, which corresponds to the range of experimentally measured SNR in this tissue. The number of performed Monte Carlo simulations was 10 000. Similar simulations were performed for WM at low SNR in the range of 5 to 40.

2.1.3 | Signal-to-noise ratio

In this work, we adopted the definition of the SNR, as described in the work by Björk et al,[37] taking into account each phase-cycled bSSFP acquisition:

$$SNR = \frac{\sum_{n=1}^{N}\left|I_n(\theta)\right|}{N\sigma} \tag{6}$$

where $\left|I_n(\theta)\right|$ is the magnitude of n^{th} phase-cycled image, σ is the SD of Gaussian noise, and N is the number of phase-cycled bSSFP acquisitions.

The minimum SNR required to achieve a SD in T_1, T_2, and Δf_0 equal to 5% of the corresponding true values was calculated for T_1 values in the range of 100 ms to 3000 ms, and for T_2 values in the range of 10 ms to 500 ms. The same initial settings for KM_0, Δf_0, δ_{CS}, φ_{RF}, and the combination of TR, FA, and N, chosen from the previously described simulations for a single-component model, were used.

2.1.4 | Experimental validation

All experiments were performed on a clinical 1.5T or 3T MR scanner (Ingenia, Philips Healthcare, Best, the Netherlands) on a calibrated phantom consisting of gel tubes with known T_1 and T_2 values (TO5, Eurospin II test system, Diagnostic Sonar Ltd, Livingston, Scotland). Twelve tubes were chosen with T_1 and T_2 combinations in the following ranges: T_1 (220 ms-1600 ms) and T_2 (50 ms-360 ms).

To investigate the performance of the method at high and low SNR levels, 3D phase-cycled bSSFP data were acquired using a 16-channel head coil (dS HeadSpine, Philips Ingenia,

Best, Netherlands) and using the integrated body coil as a receiver for high and low SNR scans, respectively. The body coil was used as a transmitter in both cases. The following sequence parameter settings were used: FOV = 220 × 220 × 60 mm^3, voxel size 1.5 × 1.5 × 3 mm^3, TR = 10 ms, TE = 5 ms, FA = 30º, number of signal averages (NSA) = 1, and 10 RF phase-increment steps with $\Delta\theta = \frac{\pi}{5}$. The total scan time was 5 minutes and 55 seconds. Complex-valued data were acquired. To minimize transient magnetization state effects, 6 seconds of dummy cycles were added before each dynamic acquisition. B_1 correction was performed voxel-wise using an additionally acquired B_1 map.[38] The SNR was calculated using Eq. (6). The noise level was measured using a double acquisition method.[39,40] Region of interest (ROI) analysis was performed on three selected reference tubes.

2.2 | Two-component phase-cycled bSSFP signal model

The complex phase-cycled bSSFP signal in the case of the two-component relaxation model can be described as a weighted complex sum of two signals, each of which is described by Eqs. (1–3):

$$I = w_1 I_1 + w_2 I_2 = w_1 M_{\text{eff},1} \cdot \frac{1-a_1 e^{i\theta_1}}{1-b_1 cos\theta_1} \cdot e^{i\varphi_1} + w_2 M_{\text{eff},2} \cdot \frac{1-a_2 e^{i\theta_2}}{1-b_2 cos\theta_2} \cdot e^{i\varphi_2} \quad (7)$$

where $M_{\text{eff},1}$, a_1, b_1 are parameters describing a first component with a volume fraction of w_1, and $M_{\text{eff},2}$, a_2, b_2 are parameters describing a second component with a volume fraction of $w_2 = 1 - w_1$.

Human brain tissue, particularly WM, is often modeled to be a two-component nonexchanging system consisting of a dominant long T_{1L} and T_{2L} component and a smaller short T_{1S} and T_{2S} component related to the presence of myelin.[20,25,41-44] The frequency distributions for both components is often taken to be Lorentzian. At 3T the dominant component is assumed to be on-resonance with a FWHM Γ_1 = 0.1 Hz, whereas the smaller component has an average frequency shift of Δf = 20 Hz and a FWHM Γ_2 = 20 Hz.[19] A volume fraction of a small component is often referred as myelin water fraction.

After substituting relaxation times and volume fractions into Eq. (7), the signal from WM can be described as

$$I = (1-MWF) \cdot M_{\text{eff},L} \frac{1-a_L e^{i(2\pi\Delta f_0 TR-\Delta\theta)}}{1-b_L \cos(2\pi\Delta f_0 TR-\Delta\theta)} \cdot e^{i(2\pi\Delta f_0 TE+\varphi_{RF})} + MWF \cdot M_{\text{eff},S} \cdot \frac{1-a_S e^{i(2\pi(\Delta f+\Delta f_0)TR-\Delta\theta)}}{1-b_S cos(2\pi(\Delta f+\Delta f_0)TR-\Delta\theta)}, \quad (8)$$

where $M_{\text{eff},L}$, a_L, b_L parameters describe the dominant long component, and $M_{\text{eff},S}$, a_S, b_S parameters describe the small component.

2.2.1 | Accuracy and precision

The accuracy and precision were assessed using Eqs. (4) and (5), with X_{true} being the true parameter values for the dominant component.

2.2.2 | Numerical simulations

To assess the accuracy and precision of the parameter estimates, Monte Carlo simulations were performed for the same range of FA, TR, and number N of RF phase increment steps as used in the case of a single-component model. The initial parameter settings were KM_0 = 10 000, Δf_0 = 10 Hz, and $\varphi_{RF} = 0$. We used the average values for T_1, T_2, and a volume fraction from literature to describe the components[19,27,28,31-33]: The dominant component is on-resonance and has T_{1L} = 1000 ms and T_{2L} = 80 ms, with a volume fraction of 0.88, and the smaller component has shift Δf = 20 Hz, T_{1S} = 400 ms and T_{2S} = 10 ms, with a myelin water fraction of 0.12. Gaussian noise was added independently to the real and imaginary data of the complex sum, resulting in an SNR ranging from 30 to 150. The number of performed Monte Carlo simulations was 1000. The PLANET single-component model reconstruction was not changed and was applied to data from a two-component tissue.

Additional noise-free simulations were performed to access the influence of the volume fraction, the frequency shift, and relaxation parameters of the two components on the accuracy of the method. Five different cases were simulated:

1. T_{1L} = 1000 ms and T_{2L} = 80 ms, volume fraction of 0.88; T_{1S} = 400 ms and T_{2S} = 20 ms, volume fraction of 0.12, shift Δf = 20 Hz
2. T_{1L} = 1000 ms and T_{2L} = 80 ms, volume fraction of 0.88; T_{1S} = 1000 ms and T_{2S} = 80 ms, volume fraction of 0.12, shift Δf = 20 Hz
3. T_{1L} = 1000 ms and T_{2L} = 80 ms, volume fraction of 0.88; T_{1S} = 400 ms and T_{2S} = 20 ms, volume fraction of 0.12, shift Δf = 0 Hz
4. T_{1L} = 1000 ms and T_{2L} = 80 ms, volume fraction of 0.5; T_{1S} = 400 ms and T_{2S} = 20 ms, volume fraction of 0.5, shift Δf = 0 Hz
5. T_{1L} = 1000 ms and T_{2L} = 80 ms, volume fraction of 0.5; T_{1S} = 400 ms and T_{2S} = 20 ms, volume fraction of 0.5, shift Δf = 20 Hz

2.2.3 | Experimental validation

To validate the simulation results for the brain tissue, experiments on five healthy volunteers on a 3T MR scanner were

performed with the following sequence parameter settings: FOV = 220 × 220 × 100 mm^3, TR = 10 ms, TE = 5 ms, FA = 20º, and NSA = 1. Parallel imaging was used with SENSE factor of 2 in the right–left direction, $N = 10$ RF phase increment steps with $\Delta\theta = \frac{\pi}{5}$, voxel size = 0.98 × 0.98 × 4 mm^3, with the total scan time of 6 minutes and 14 seconds. Complex-valued data were acquired. To minimize transient effects, 10 seconds of dummy cycles (1000 RF pulses) were added before each dynamic acquisition. A 2.5-ms-long RF excitation pulse was used to minimize magnetization effects.[45] B_1 correction was performed voxel-wise using an additionally acquired B_1 map.[38]

Reference T_1 and T_2 maps of the brain were calculated on one volunteer on a 3T MR scanner. For the reference T_1 mapping, a 2D turbo inversion-recovery spin-echo approach was used with TR = 7000 ms, TI = [50, 100, 200, 400, 800, 1600, 3200] ms, with the following nonlinear fit of $S(TI) = \rho\left|1 - \alpha e^{-TI/T_1}\right|$ to multi-TI inversion-recovery spin-echo data (with α related to imperfect inversion pulses). For the reference T_2 map, a 2D multi-echo spin-echo approach was used with TR = 5000 ms, TE = [20, 40, 60, 80, 100, 120, 140, 160] ms, with the following nonlinear fit of $S(TE) = \rho e^{-TE/T_2}$ to multi-echo spin-echo data using all acquired echoes.

The ROI analyses were performed on the quantitative T_1 and T_2 maps calculated for five healthy volunteers at 3T. The ROIs in WM (each approximately 70 voxels) were placed manually in the frontal and occipital parts in each hemisphere. The ROIs in gray matter (each approximately 20 voxels) were placed manually in peripheral parts of each hemisphere.

2.3 | Gibbs ringing analysis

2.3.1 | Numerical simulations

To investigate the influence of Gibbs ringing artifacts on parameter maps estimated using PLANET, we performed simulations using a numerical brain phantom.[46] The T_1, T_2, proton density, and Δf_0 maps of one axial slice of the brain were generated. Using the combination of FA, TR, number N of RF phase increment steps chosen from the previously described simulations, and generated maps, the complex single-component phase-cycled bSSFP signal was calculated using the model in Eq. (1). Gaussian noise was added to achieve realistic SNR values, similar to those in our experimental setups (approximately 150-200). Pseudo-infinite Cartesian *k*-space was generated using 2D fast Fourier transform (matrix size = 1000 × 1000). Subsequently, different reconstructions of *k*-space data were performed to create Gibbs ringing artifacts of varying severity:

1. Two-dimensional inverse fast Fourier transform was performed on the fully simulated *k*-space. The quantitative maps were estimated using the PLANET method (no Gibbs ringing).
2. Before computing 2D inverse fast Fourier transform, *k*-space truncation was performed, corresponding to a low-resolution acquisition matrix of 132 × 132.
3. Before computing 2D inverse fast Fourier transform, *k*-space truncation was performed, corresponding to a high-resolution acquisition matrix of 512 × 512.

In case 1 there is no Gibbs ringing produced, whereas for cases 2 and 3 some degree of Gibbs ringing was expected and the Gibbs ringing artifact removal method based on local subvoxel shifts, proposed by Kellner et al,[47] was applied before applying the PLANET parameter estimation method. No apodization on *k*-space was applied.

2.3.2 | Experimental validation

To validate the Gibbs ringing effects, experimental 3D phase-cycled bSSFP data were acquired on the phantom and in vivo on the brain of a healthy volunteer on a 1.5T MR scanner. Different acquisition voxel sizes were used under the same sequence parameter settings (TR, TE, FA, and FOV were equal). To remove the Gibbs-ringing artifacts, a method based on resampling of the image based on local subvoxel shifts[47] was additionally applied before performing the PLANET reconstruction for all setups. For the phantom, the following sequence parameter settings were used: FOV = 220 × 220 × 81 mm^3, TR = 10 ms, TE = 5 ms, FA = 30º, NSA = 1, $N = 10$ RF phase increment steps with $\Delta\theta = \frac{\pi}{5}$, voxel size 1.96 × 1.96 × 3 mm^3, and 0.98 × 0.98 × 3 mm^3 for the low and high spatial resolution with a total scan duration of 6 minutes and 3 seconds, and 10 minutes and 54 seconds, respectively. Six seconds of dummy cycles were added before each dynamic acquisition. For the brain the following sequence parameter settings were used: FOV = 220 × 220 × 100 mm^3, TR = 10 ms, TE = 5 ms, FA = 20º, NSA = 1, $N = 10$ RF phase increment steps with $\Delta\theta = \frac{\pi}{5}$, and voxel size = 1.53 × 1.53 × 4 mm^3 and 0.98 × 0.98 × 4 mm^3 for the low and high spatial resolution, with the total scan time of 7 minutes and 39 seconds, and 10 minutes and 59 seconds, respectively. To minimize transient effects, 10 seconds of dummy cycles were added before each dynamic acquisition. Complex-valued data were acquired, and no B_1 correction was performed for both cases.

All simulations and calculations were performed in MATLAB R2015a (The MathWorks Inc, Natick, MA).

To minimize eddy-currents effects, a linear phase-encoding profile order was used, as suggested by Bieri et al,[48] for all experimental setups.

3 | RESULTS

3.1 | Single-component phase-cycled bSSFP signal model

3.1.1 | Simulation results

The ellipse fitting step is an important part of the PLANET method.[17] The performance of this fitting procedure depends on the shape of the ellipse, which depends on the relaxation times but also on the chosen FA and TR combination. Figure 1 shows a schematic example of geometrical shape of an ellipse and its location in the complex signal plane for different FA and TR combinations for $T_1 = 830$ ms and $T_2 = 80$ ms, representing WM at 3T. To make a comparison easier, the case of $\Delta f_0 = 0$, $\delta_{cs} = 0$, and $\varphi_{RF} = 0$ is shown, which corresponds to the vertical form of an ellipse.

For low FA, the ellipse is elongated and approaches the limit case when $FA = \cos^{-1}(E_1)$, which corresponds to a collapse of an ellipse to a line (case FA = 9° and TR = 10 ms), where the ellipse fitting would fail and parameters cannot be properly estimated. This FA is the Ernst angle: $FA_E = \cos^{-1}\left(\exp\left(-TR/T_1\right)\right)$. As suggested,[17] the correct choice of FA should be done by choosing $FA > \cos^{-1}\left(\exp(-TR/T_{1shortest})\right)$. For high FA, the ellipse approaches a circle (where semi-axis A is equal to semi-axis B),

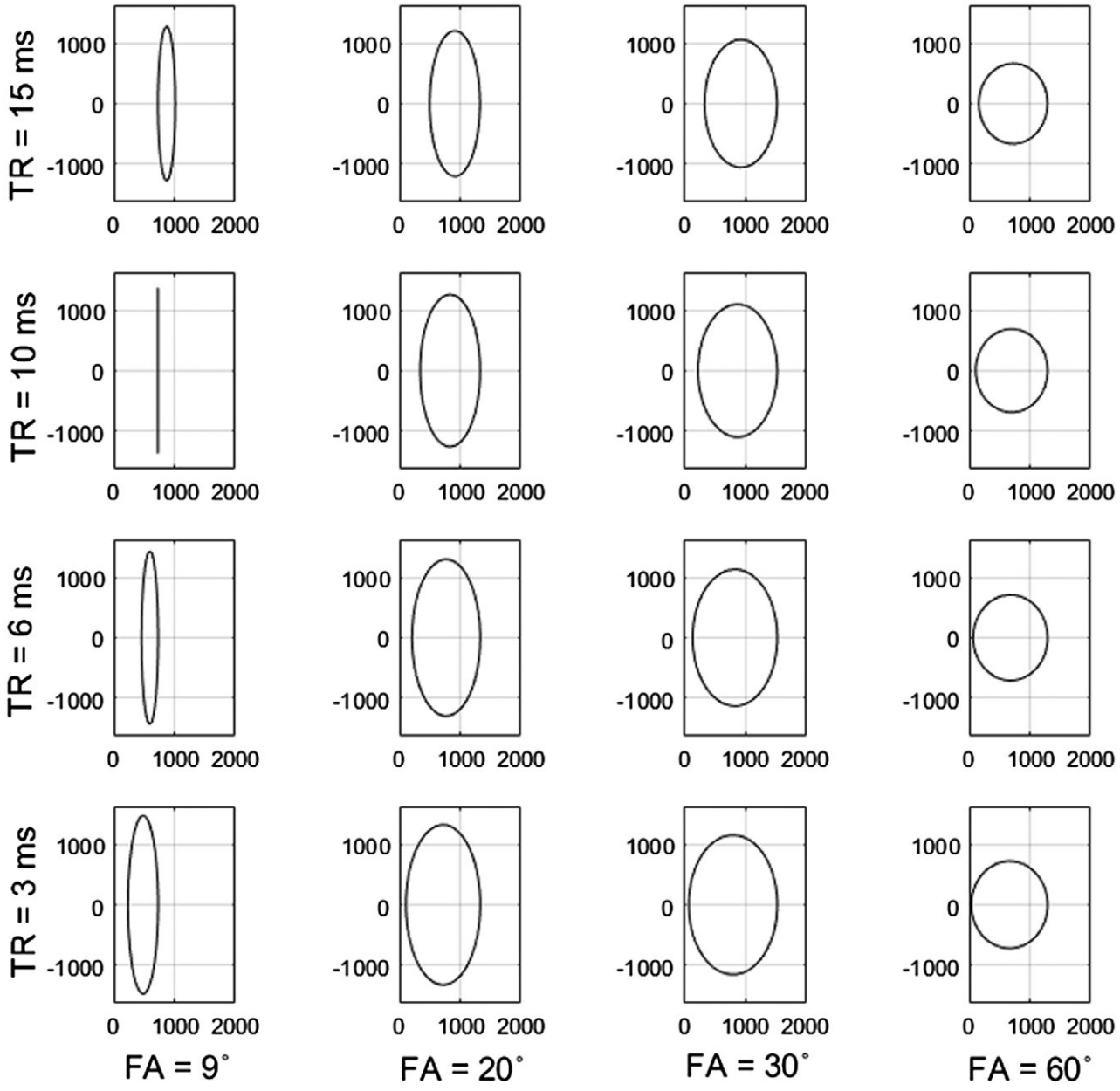

FIGURE 1 Illustration of the dependence of the geometrical shape and location of an ellipse on the flip angle (FA) and TR in the complex signal plane. Example shown for $T_1 = 830$ ms, $T_2 = 80$ ms. $\Delta f_0 = 0$, and $\varphi_{RF} = 0$

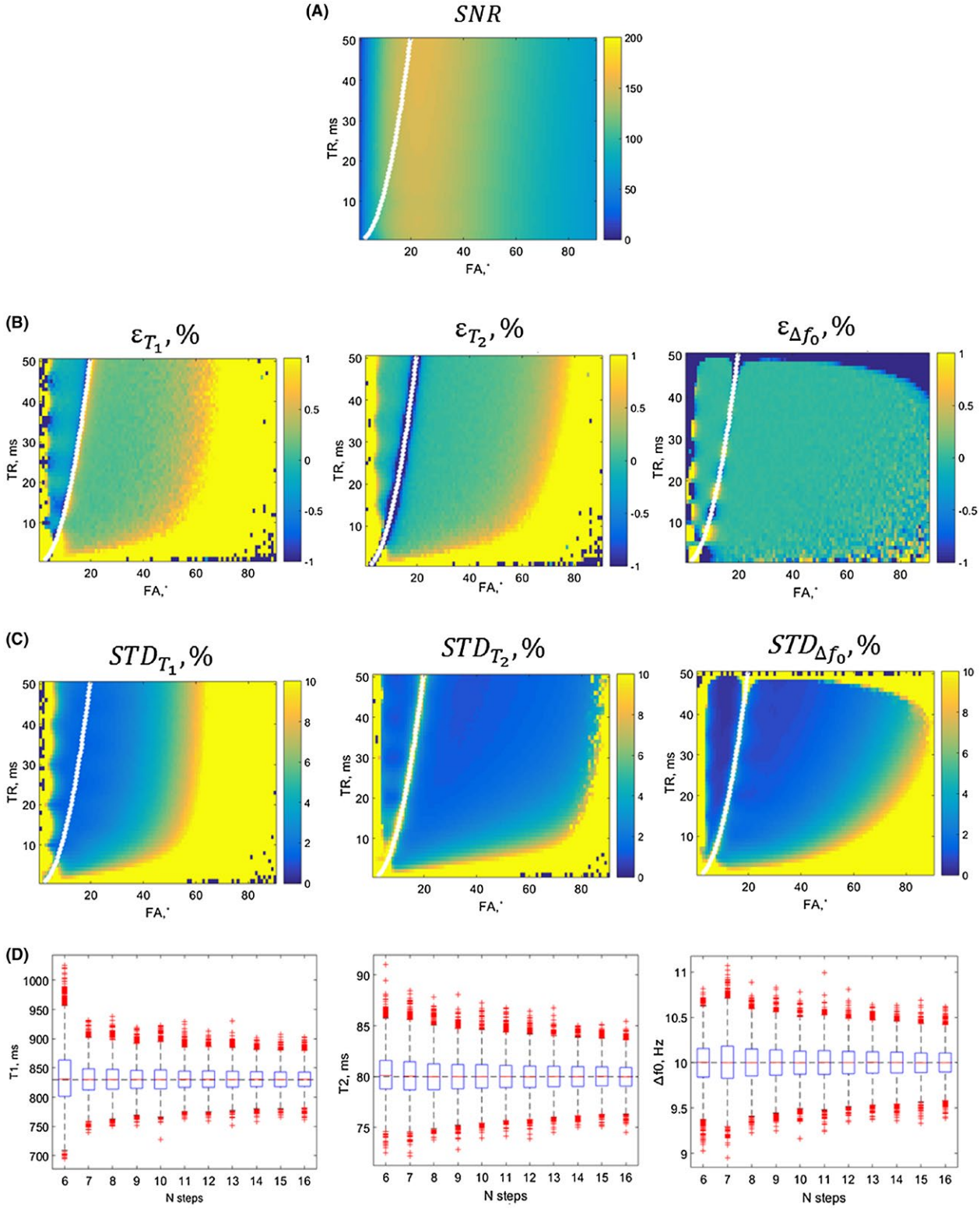

FIGURE 2 Simulation results for a single-component white matter (WM) model at 3T (T_1 = 830 ms, T_2 = 80 ms) and Δf_0 = 10 Hz. Ten RF phase increment steps: SNR as a function of FA and TR (A); relative errors ε (in percent) in all parameter estimates compared with their true values (B); standard deviation STD (in percent) of all parameter estimates compared with their mean values (the white line corresponds to FA = FA_E; only the region to the right is allowed) (C); and distribution of all parameter estimates in the boxplots as a function of the number of RF phase increment steps *N* (D). Black dashed lines correspond to the true parameter values

which can only be achieved if $E_2 = 1$ or $T_2 \to \infty$, as shown by Xiang et al in the Appendix.[34] For short TR, the ellipse is located very close to the origin. In cases with considerable noise the fitting can be such that the origin is inside the ellipse, which results in obviously erroneous negative T_1 and T_2 estimates. The use of longer TR shifts the ellipse along the real axis, avoiding the described situation; however, it also results in a longer acquisition duration. Based on these observations, we suggest that the optimal elliptical shape for fitting is obtained using TR greater than 6 ms and FA approximately equal to 20º to 30º.

An analysis of the SNR, relative errors, and SDs in T_1, T_2, and Δf_0 estimates for a single-component WM is presented in Figure 2. The SNR is calculated using Eq. (6) for different combinations of FA and TR and is shown in Figure 2A. The high SNR values can be achieved for FA in a range of 20º to 30º. As shown in Figure 2B,C, there is a broad "sweet spot" of TR and FA combinations, with high accuracy and precision in T_1, T_2, and Δf_0 estimates. A small bias in T_1 and T_2 parameter estimates can be observed (Figure 2B). For FA greater than FA_E, the T_1 and T_2 values are overestimated.

The distributions of the parameter estimates as a function of the number of RF phase increment steps N are compared in the boxplots of Figure 2D. Increasing the number N from 6 to 8 improves the precision in all parameter estimates; however, increasing N further does not influence the precision in the estimates much. The results of the analysis for WM at low SNR levels are presented in Supporting Information Figure S1.

The minimum SNR required to achieve a SD of T_1, T_2, and Δf_0 parameter estimates equal to 5% of their mean values is shown in Figure 3. It can be seen that the minimum required SNR depends on the T_1 and T_2 values themselves. For example, to estimate T_1 values of approximately 800 ms, T_2 values of approximately 80 ms, and Δf_0 of approximately 20 Hz, with 5% relative SD in the corresponding parameter estimates compared with their mean values, a corresponding SNR of 80, 60, and 30 is required.

3.1.2 | Experimental results

Figure 4A,B shows the phantom results at different SNR levels: SNR maps, a banding free magnitude image, and

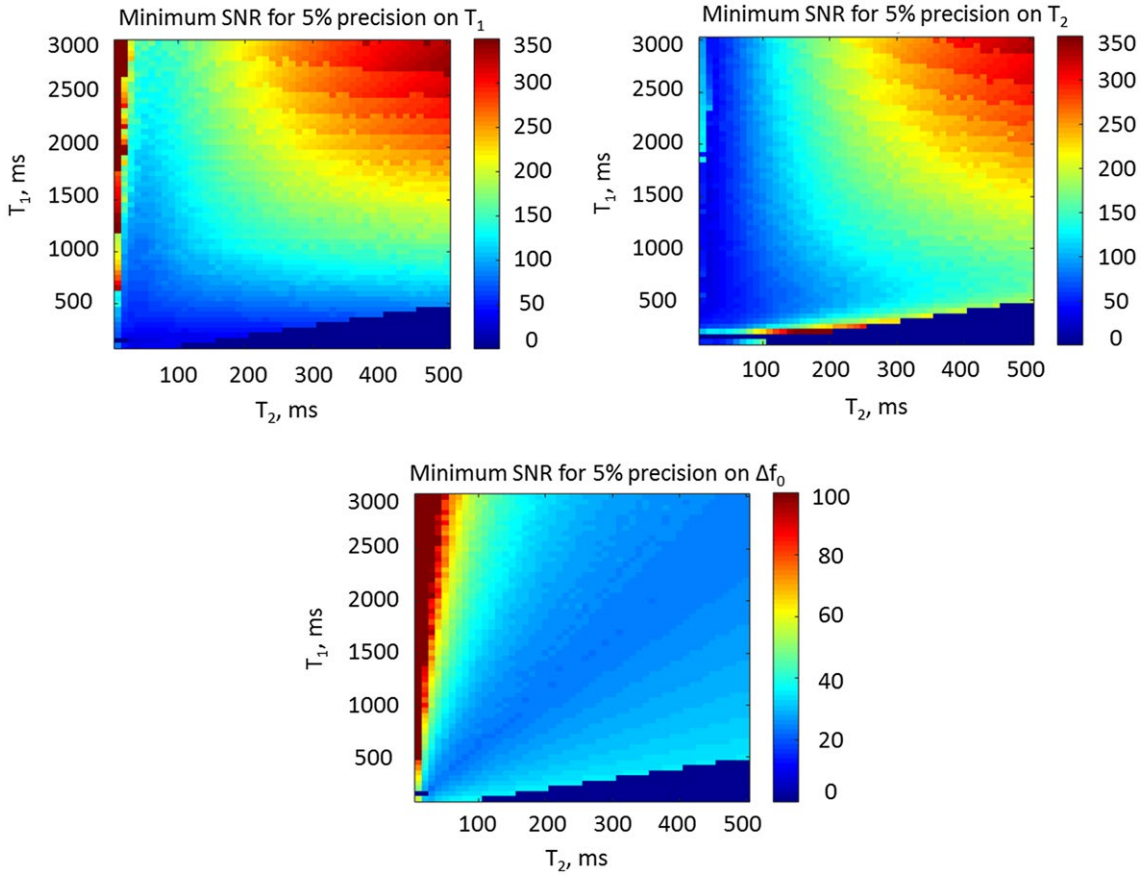

FIGURE 3 Minimum SNR required to achieve a precision of 5% of the mean values of the parameters T_1, T_2, and Δf_0. The initial sequence parameter settings were TR = 10 ms, FA = 20º, Δf_0 = 20 Hz, and N = 10 RF phase increment steps. The values $T_1 < T_2$ are excluded (blue). Note that the SNR range for precision in T_1 and T_2 is saturated at 350, and in Δf_0 at 100

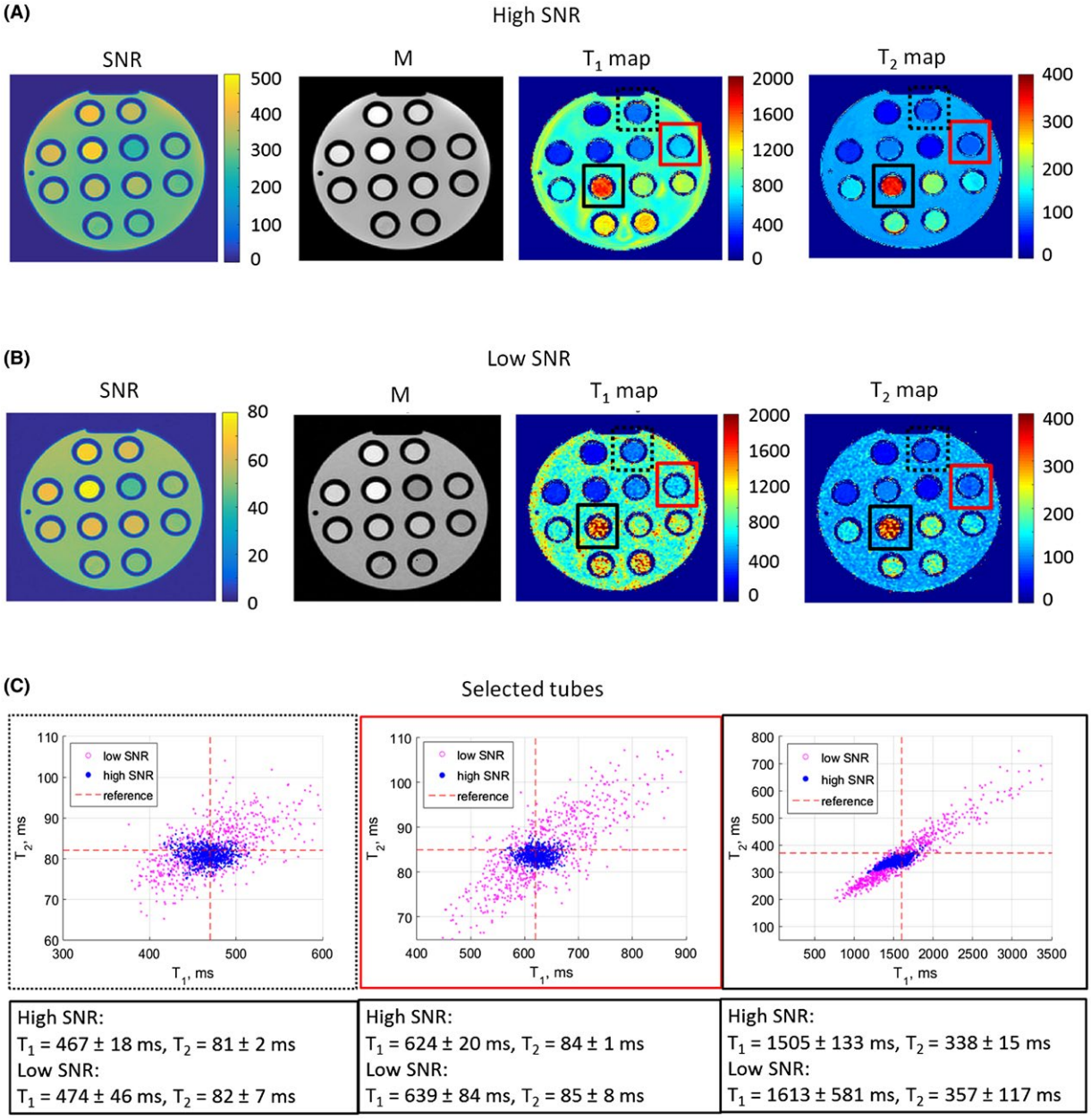

FIGURE 4 Experimental results from the phantom study. A, Signal-to-noise ratio map, banding free magnitude image, T_1 and T_2 maps, calculated using the PLANET method at high SNR level (using a head coil). B, Signal-to-noise ratio map, banding free magnitude image, T_1 and T_2 maps, calculated using the PLANET method at low SNR level (using the integrated body coil). C, Scatterplot of T_1 and T_2 estimates over a region of interest inside 3 selected tubes (black dashed, red solid, and black solid squares) for high and low SNR levels and the average calculated relaxation times for the selected tubes

T_1 and T_2 maps are presented for the different coils used. The scatterplots of the parameter estimated within ROIs are shown in Figure 4C. The average calculated relaxation times for high and low SNR levels are also shown, and they match the predictions of the performed simulations (the SD in the estimated parameters should be less than 5% of their mean values at high SNR and approximately 10% to 15% of their mean values at low SNR). The artifacts in the T_1 maps in the background fluid are caused by the artifacts in the B_1 map, which is shown in Supporting Information Figure S3.

3.2 | Two-component phase-cycled bSSFP signal model

3.2.1 | Simulation results

Figure 5A,B shows a schematic example of an ellipse observed in the case of a two-component model and corresponding frequency distributions used in the simulations. The SNR values, relative errors, and SDs in the T_1, T_2, and Δf_0 estimates are presented in Figure 5 for a two-component

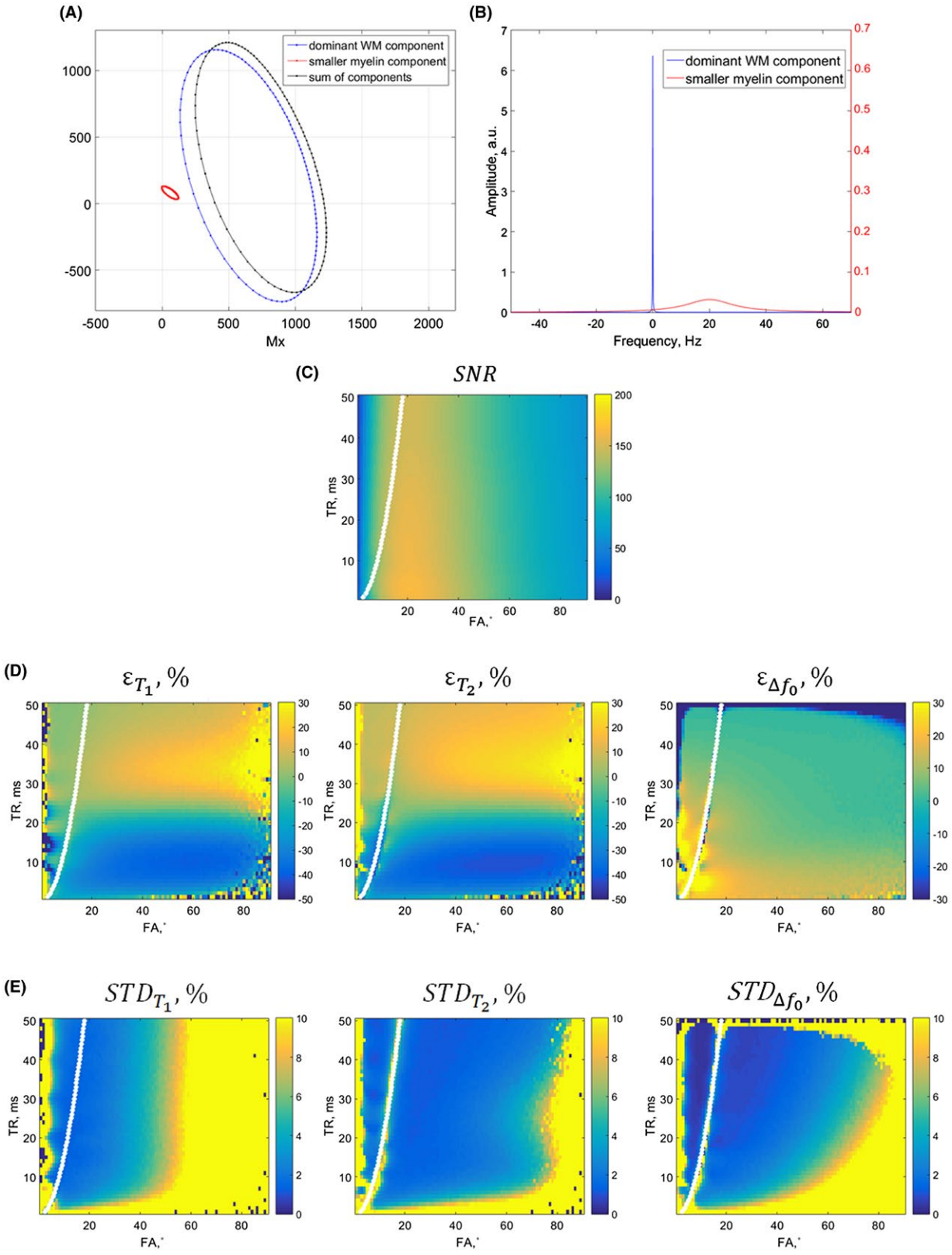

FIGURE 5 Simulation results for a two-component WM model at 3T (T_{1L} = 1000 ms, T_{2L} = 80 ms, T_{1S} = 400 ms, T_{2S} = 20 ms, and myelin water fraction = 0.12). A, Schematic representation of the observed ellipses for TR = 10 ms, FA = 20, Δf_0 = 10 Hz, and φ_{RF} = 0. B, Frequency distributions for both components used in the simulations. C, Signal-to-noise ratio as a function of FA and TR. D, Relative errors ε (in percent) in T_1, T_2, and Δf_0 estimates compared with the true values (of the dominant component). E, Standard deviation STD (in percent) in T_1, T_2, and Δf_0 estimates compared with their mean values (of the dominant component). The results are presented for N = 10 RF phase increment steps used

model (Figure 5C-E). The errors in the parameters are related to the presence of the second component and are defined as the deviation from the true values of the corresponding parameters of the dominant component. The ellipse of the smaller component interferes with the ellipse of the dominant WM component. The fitting of a single-component ellipse to the complex sum of the two ellipses results in systematic underestimation of T_1 and T_2 parameters, which depends on the choice of TR and FA, shown in Figure 5. For example, a combination of TR = 10 ms and FA = 20º leads to underestimation of T_1 by approximately 30%, underestimation of T_2 by approximately 35%, and overestimation of Δf_0 by approximately 10%. However, precision of the parameter estimates stays within the 3% range for this combination of FA and TR.

The relative errors in parameter estimates, simulated for different combinations of the volume fraction, frequency shift, and relaxation times of the components, are shown in Supporting Information Figure S2.

The errors depend on the relaxation times of the smaller component. The case in which the smaller component has shorter relaxation times is presented in Supporting Information Figure S2A, and the results for equal relaxation times are shown in Supporting Information Figure S2B. The errors increase with increasing relaxation times of the smaller component.

If there is no frequency shift between the components, the ellipses of both components have the same orientation, and their complex sum will remain an ellipse with the same orientation and with the T_1 and T_2 in between the respective T_1 and T_2 values of both components. It is a "clear" partial volume effect in this case. Small errors in T_1 and T_2 can be observed (Supporting Information Figure S2C), which increase with increasing volume fraction of the second component (Supporting Information Figure S2D). The Δf_0 estimates are quite accurate, which is expected due to the same orientation of both ellipses.

The biggest relative errors in the estimated T_1, T_2, and Δf_0 can be observed for the case of equal volume fractions of the component (which is an exaggeration of the realistic case) in combination with a frequency shift (Supporting Information Figure S2E).

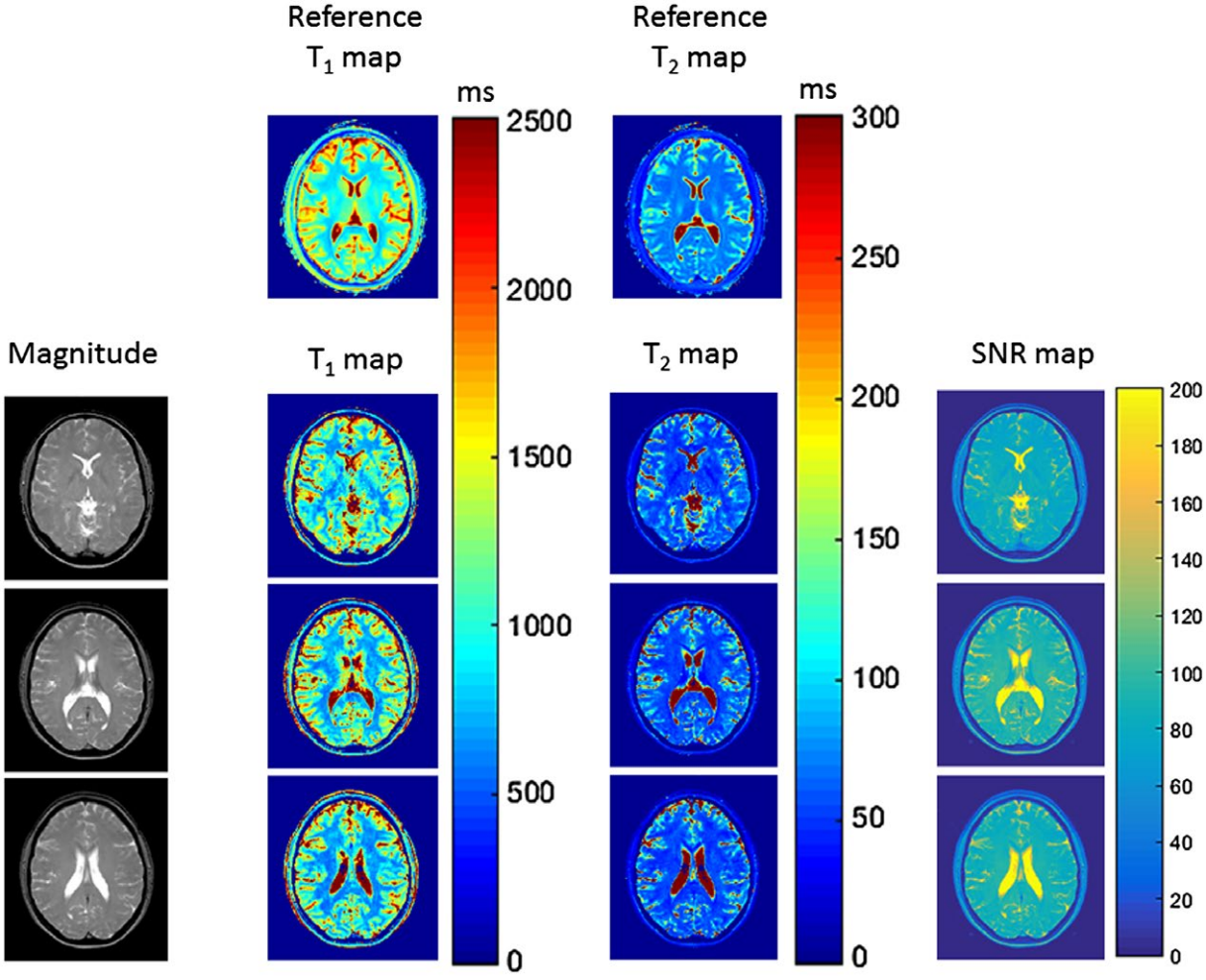

FIGURE 6 Experimental results from the volunteer study: reference T_1 and T_2 maps of one axial slice of the brain, the banding free magnitude images, the estimated T_1 and T_2 maps, and calculated SNR maps for three axial slices of the brain

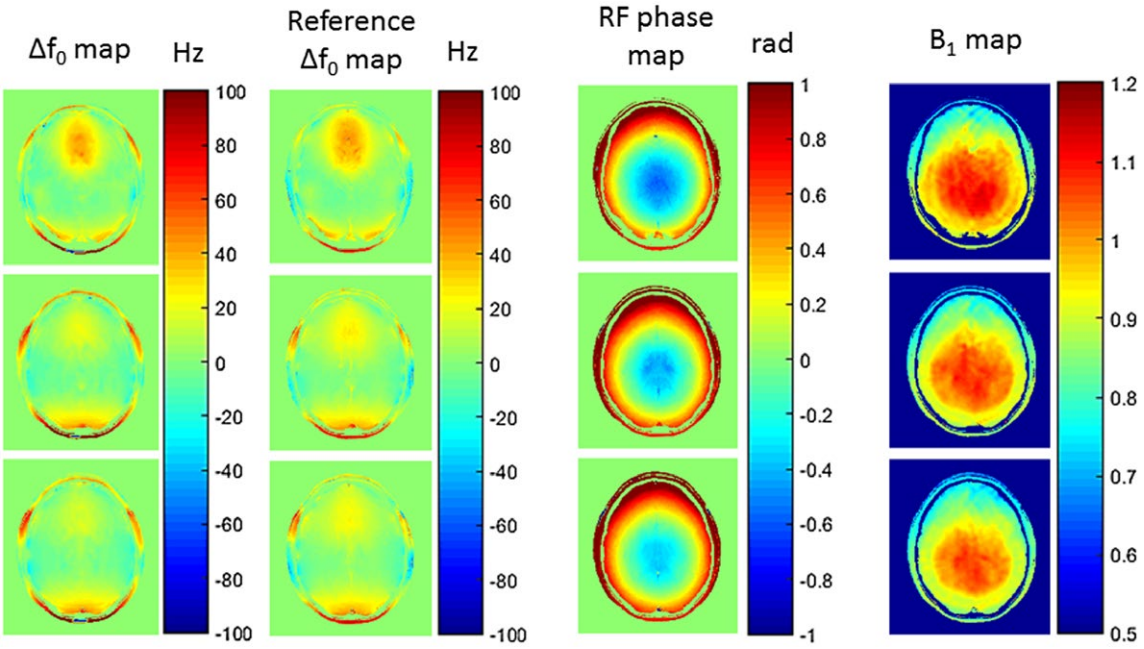

FIGURE 7 Experimental results from the volunteer study: the estimated and the reference off-resonance maps, the estimated RF phase maps, and the additionally acquired B_1 maps for three axial slices of the brain

3.2.2 | Experimental results

The quantitative maps calculated for human brain at 3T are shown in Figure 6. The reference T_1 and T_2 maps are presented for one middle axial slice. The banding free magnitude images, the maps of T_1 and T_2, are shown for three axial slices. Image registration (rigid) and Gibbs ringing filtering was applied to all data before performing the PLANET reconstruction.

The estimated and reference f_0 maps, the estimated RF phase maps, as well as B_1 maps used for FA correction are shown in Figure 7 for the same three axial slices of the brain.

The results of the ROI analysis are given in Table 1. The reference values, calculated by placing the ROIs on the reference T_1 and T_2 maps acquired on volunteer 4, are provided for comparison, as well as the values published in literature and reviewed by Bojorquez et al.[49]

3.3 | Gibbs ringing analysis

3.3.1 | Simulation results

Figure 8 shows the results of Gibbs ringing simulations on a numerical brain phantom. Banding free magnitude, and T_1 and T_2 maps of one slice are presented for different reconstructions of *k*-space data. For the low acquisition matrix of 132 × 132, the Gibbs ringing artifacts on the reconstructed quantitative maps were the most pronounced and were minimized after the correction. For the high acquisition matrix of 512 × 512, the Gibbs ringing artifacts were less visible and disappeared after the correction. The distributions of T_1 and T_2 estimates in histograms and in boxplots are shown in Supporting Information Figure S4. The results are presented for 3 cases: fully simulated *k*-space, and truncated *k*-space to low and high acquisition matrix sizes (132^2 and 512^2, respectively). Additionally, for both truncated *k*-space cases, the Gibbs ringing correction[47] was performed after reconstruction before applying PLANET. Visually, no influence of Gibbs ringing was seen in the reconstructed off-resonance maps. For this reason, we did not include the off-resonance maps in the analysis.

3.3.2 | Experimental results

The quantitative maps of the phantom and the brain calculated using the PLANET method with different reconstructions of *k*-space (low and high resolution) are presented in Figure 9. The phantom has many sharp signal transitions and all quantitative maps, calculated from the low-resolution data, suffer from severe Gibbs ringing artifacts, which are minimized after correction (Figure 9A). Still, there are inhomogeneous regions inside almost all tubes in the quantitative maps. The quantitative maps, calculated from the high-resolution data, do not suffer from Gibbs ringing artifacts, and a minor smoothing effect can be observed after correction. As shown in Figure 9B, there are fewer sharp signal transitions in the brain compared with the phantom, and Gibbs ringing does not affect the quantitative parameter maps much at all.

TABLE 1 Results from in vivo experiments: T_1 and T_2 values determined using the PLANET method and using the reference method compared with literature published values

		PLANET				Literature published values*			
		White matter		Gray matter		White matter		Gray matter	
Volunteer No.	ROI	T_1, ms	T_2, ms	T_1, ms	T_2, ms	T_1, ms	T_2, ms	T_1, ms	T_2, ms
Volunteer 1	1	657 ± 71	54 ± 5	1128 ± 71	65 ± 5	832 ± 1 (36)	80 ± 1 (36)	1331 ± 31 (36)	110 ± 2 (36)
	2	686 ± 61	55 ± 5	1125 ± 73	68 ± 8	1084 ± 45 (22)	69 ±3 (22)	1820 ± 114 (22)	99 ± 7 (22)
	3	640 ± 40	52 ± 4	1095 ± 99	69 ± 8	840 ± 50 (50)	75 ± 3 (51)	1600 ± 110 (50)	83 ± 4 (51)
	4	664 ± 40	51 ± 5	1056 ± 53	64 ± 5	1110 ± 40 (52)	65 ± 6 (53)	1470 ± 50 (52)	109 ± 11 (53)
	5	691 ± 45	53 ± 4			532 ± 56 (16)	44 ± 5 (16)	1061 ± 169 (16)	63 ± 12 (16)
	6	647 ± 47	51 ± 4			1085 ± 64 (54)		1717 ± 61 (54)	
Volunteer 2	7	664 ± 51	50 ± 5	1070 ± 71	64 ± 7	1433 ± 80 (55)		968 ± 85 (55)	
	8	668 ± 67	54 ± 4	1172 ± 82	70 ± 6	954 ± 39 (41)			
	9	695 ± 32	53 ± 6	1102 ± 95	71 ± 10	781 ± 61 (53)			
	10	696 ± 58	52 ± 3	1080 ± 84	60 ± 7				
	11	700 ± 38	53 ± 6						
Volunteer 3	12	664 ± 61	51 ± 6	1185 ± 84	68 ± 9				
	13	623 ± 47	51 ± 6	1082 ± 99	66 ± 12				
	14	603 ± 49	50 ± 5	1129 ± 94	59 ± 12				
	15	686 ± 58	51 ± 5	1049 ± 51	63 ± 10				
	16	635 ± 58	50 ± 4	1036 ± 63	60 ± 9	Reference values† from 2D IR-SE and 2D ME-SE			
	17	678 ± 64	51 ± 5			White matter		Gray matter	
	18	669 ± 49	50 ± 3			T_1, ms	T_2, ms	T_1, ms	T_2, ms
Volunteer 4	19	670 ± 37	50 ± 4	1128 ± 91	58 ± 6	824 ± 14	69 ± 3	1135 ± 34	70 ± 3
	20	661 ± 51	51 ± 4	1051 ± 90	57 ± 7	810 ± 14	70 ± 2	1132 ± 42	69 ± 3
	21	644 ± 37	53 ± 4	1076 ± 63	57 ± 5	836 ± 17	74 ± 4	1180 ± 53	74 ± 3
	22	636 ± 45	50 ± 4	1052 ± 61	58 ± 3	811 ± 24	77 ± 5	1118 ± 29	67 ± 6
	23	652 ± 36	54 ± 4			817 ± 24	74 ± 4	1170 ± 58	75 ± 5
						809 ± 29	74 ± 3	1148 ± 39	65 ± 5
Volunteer 5	24	654 ± 52	53 ± 4	1113 ± 99	70 ± 10				
	25	660 ± 45	52 ± 5	1043 ± 68	68 ± 6				
	26	687 ± 41	51 ± 5	1139 ± 99	70 ± 14				
	27	693 ± 48	51 ± 5	1110 ± 97	72 ± 15				
	28	684 ± 45	55 ± 4						
	29	659 ± 46	53 ± 4						
	30	664 ± 64	50 ± 5						
	Mean	664 ± 58	52 ± 5	1096 ± 91	65 ± 10	818 ± 21	73 ± 4	1147 ± 43	70 ± 4

Abbreviations: IR-SE, inversion recovery spin echo; ME-SE, multi-echo spin echo; ROI, region of interest.

*Numbers in parentheses are reference citations.

†Reference values calculated by placing ROIs on the reference T_1 and T_2 maps acquired on a volunteer #4.

4 | DISCUSSION

The proper choice of the sequence parameters such as FA, TR, and number of RF phase increment steps results in more accurate and precise estimation of the relaxation times T_1 and T_2, and the off-resonance Δf_0 using the PLANET method.

For a single-component signal model the settings of FA and TR along with the relaxation times T_1 and T_2 determine the shape of the ellipse. As shown in Figure 1, the ellipse should be elongated (FA = 20º to 30º) and shifted further from the origin (TR > 6 ms) to achieve robust fitting in the presence of noise. The simulation results in Figure 2 show that there is a broad "sweet spot" of TR, FA, and number of

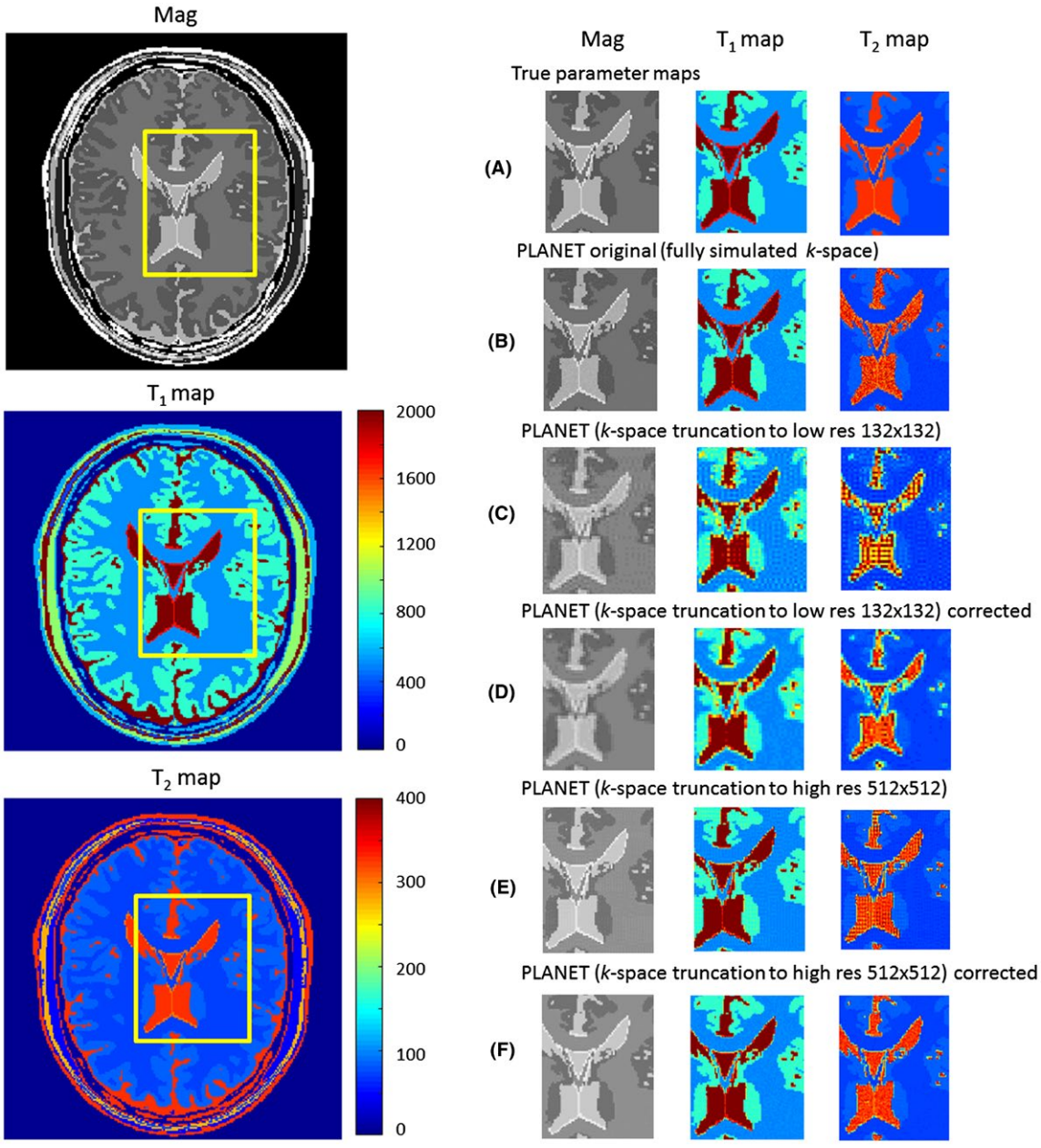

FIGURE 8 Results of simulations on a numerical brain phantom: banding free magnitude M and relaxation parameters T_1 and T_2 for the different cases. A, True parameter maps. B-F, Parameter maps calculated using PLANET: on fully simulated *k*-space (B), on truncated *k*-space to low-resolution matrix 132×132 (C,D) with additionally applied Gibbs ringing correction (D), and on truncated *k*-space to high-resolution matrix 512×512 (E,F) with additionally applied Gibbs ringing correction (F)

RF phase increment steps with a high accuracy and precision in all parameter estimates. However, a small bias observed in T_1 and T_2 estimates (see Figure 2B for $FA > FA_E$) may be caused by the ellipse fitting method, which was shown to be biased toward smaller ellipses due to the use of algebraic distances of points.[50]

The properly chosen combination of these sequence parameters should work for a wide range of relaxation times, as shown in Supporting Information Table S1. This can be of importance when trying to detect changes in relaxation times due to pathology in the tissues.

The combination of FA of 20º and TR of 10 ms appears to be a proper choice for a single-component signal model to estimate T_1 in the range of 200 ms to 3000 ms, and T_2 in the range of 50 ms to 500 ms, with a high accuracy and precision at realistic SNRs. The optimal choice for TR is different compared with that for conventional bSSFP imaging, in which TR is usually set to be shortest to minimize banding artifacts. Using a longer TR results in improved precision and accuracy when using PLANET, but also in more banding artifacts on the magnitude source images. However, these are successfully removed in the reconstruction of the banding free magnitude

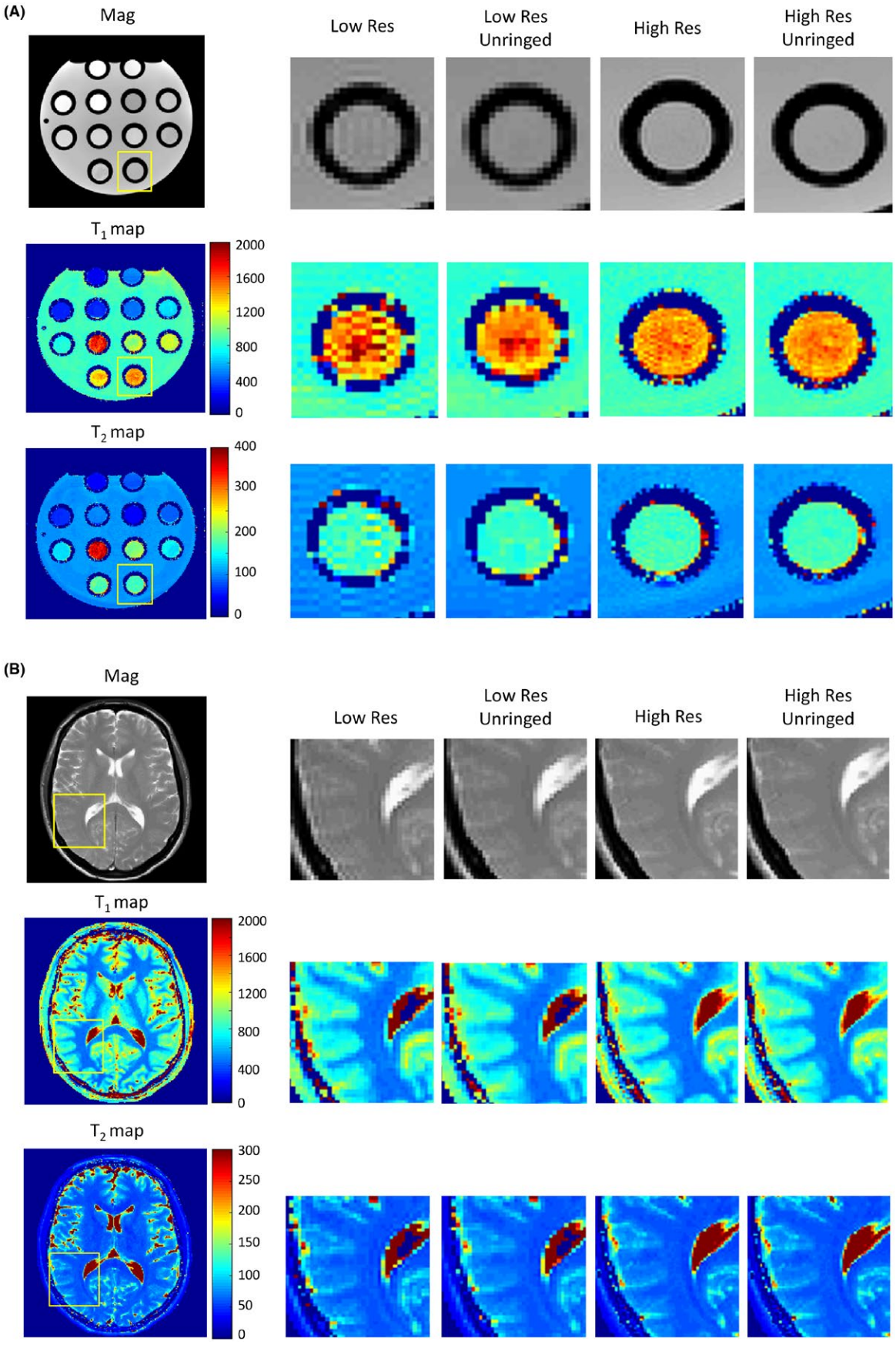

FIGURE 9 Quantitative maps of the phantom (A) and of the brain (B), calculated using the PLANET method for low-resolution and high-resolution scans with and without Gibbs ringing filtering

image. For these reasons, for speeding up PLANET, the use of a longer TR in combination with an acceleration technique that sacrifices SNR for speed, like parallel imaging, is a better choice than making use of a short TR.

Based on the number of degrees of freedom in the ellipse fitting procedure, the minimally required number of RF phase increment steps is 6. This would be enough for accurate parameter estimation using data without noise, but for realistic SNRs (100-250 in the performed experiments) the precision in the estimated parameters increases when the number of RF phase increment steps is increased. Interestingly, the precision does not further increase much more than 10 RF phase increment steps. The accuracy does not depend on the number of RF phase increment steps much. Therefore, using 8 to 10 RF phase increment steps is sufficient, as using more RF phase increment steps results in a longer acquisition time and does not influence the precision.

The minimum SNR required to achieve a precision of 5% of the mean values in T_1, T_2, and Δf_0 estimation using the optimized TR/FA/*N* cycles combination is lower than what we typically obtained in the phantom (average SNR of 250) for a voxel size of $1.4 \times 1.4 \times 3$ mm^3 and in vivo (average SNR = 150) for a voxel size of $1.5 \times 1.5 \times 4$ mm^3. Interestingly, similar results were found in the work by Björk et al[37] for the minimum required SNR; however, they concluded that the application of their method was not feasible at common SNRs, which were rather low in their work. However, they calculated the minimum SNR to achieve the precision of 5% of the true parameter values, not the mean.

For a two-component system like WM, however, the use of the optimal parameter combination defined previously would result in underestimation of T_1 and T_2 values. Unlike a single-component relaxation model, a two-component model describes the signal as a complex sum of weighted signals from the two components with different frequency distributions and different relaxation parameters. The frequency shift between the components in combination with the difference of their volume fractions causes asymmetries in the bSSFP profile, which has an effect on the performance of the method. The ellipse of the dominant component is disturbed by the presence of the second component. Their weighted complex sum generally does not have an elliptical shape and cannot be fitted as an ellipse. However, the myelin component has shorter relaxation times and a smaller volume fraction than the main component has, and their weighted complex sum can still be fitted reasonably well as an ellipse, but with different "observed" T_1 and T_2 values.

In simulations we used the frequency shift between the dominant and myelin components $\Delta f = 20$ Hz, which is the average value between those corresponding to different tract orientation in WM at 3T $\Delta f = 23 \pm 3$ Hz [$\perp$B0] and $\Delta f = 17 \pm 7$ Hz [$\parallel$ B0]).[19] We did not take into account the other sources that could contribute to the frequency shifts between the components in WM, like nonheme iron, proteins, lipids, and deoxyhemoglobin.[19]

The experimentally observed in WM mean T_1 value is 664 $\pm$ 58 ms, and the mean T_2 value is 52 $\pm$ 5 ms. The values are underestimated by approximately 30% compared with the reference and literature published values at 3T (Table 1). Similar underestimation of T_1 and T_2 is also observed from the simulation results (Figure 5), and depends on the choice of FA and TR. The presented results suggest that the PLANET method can be sensitive for detecting demyelination in human brain, which should be further investigated.

It might be interesting to investigate a different two-component model fitting approach for WM, which can be described with a set of 13-14 parameters (2 elliptical models, each described with 6 polynomial coefficients, a certain frequency shift and the volume fraction of the smaller component). To solve for all of these parameters, the measurements have to be performed at least with 2 or 3 different settings for TE and TR, maybe trying to suppress the smaller component. This different fitting approach is much more complex and goes beyond the scope of the current paper.

For a single-component model, the off-resonance maps can be calculated with a high accuracy and a high precision even at short TR (3-5 ms) for different tissue types at SNR levels of approximately 30. However, for a two-component model, the off-resonance maps are overestimated by approximately 10% (TR ~ 10 ms) with a precision within 2% for a wide TR-FA range.

The truncation of *k*-space during the acquisition leads to Gibbs-ringing artifacts, the severity of which depends on the acquisition voxel size. Additionally, the use of RF phase cycling shifts banding artifacts between the acquired bSSFP phase-cycled data and leads to different Gibbs ringing appearance. As shown in Figure 8 and Supporting Information Figure S4, this effect can result in additional systematic errors in the quantitative parameters even for a properly chosen sequence parameter combination. We therefore suggest using a high acquisition matrix in combination with a suitable method for removal of Gibbs ringing artifacts to improve the precision and accuracy of the parameter estimates, when PLANET is applied to a phantom. For in vivo use, a relatively high acquisition matrix should be enough to minimize Gibbs ringing artifacts.

We focused primarily on the application of PLANET in the brain, where the high SNR can be achieved easily on a 1.5T or 3T clinical MR scanner with a regular coil setup, which is important for clinical use. Given the optimal settings, 1-mm^3 isotropic whole-brain T_1, T_2, M, and Δf_0 mapping (with FOV = $220 \times 220 \times 100$ mm^3) can be performed within a 10-15-minute scan time (with SENSE factor of 2). This duration is comparable with that of DESPOT1- and DESPOT2-based T_1 and T_2 mapping.[8,9] The clear benefit of PLANET is that in addition to quantitative T_1 and T_2 maps we can estimate the off-resonance map, the RF phase map, and reconstruct the banding free magnitude image.

For applications in the abdomen, where considerable motion is present, the current implementation of the method is not fast

enough. The use of a different readout trajectory or an acceleration technique, as well as the use of a 2D approach, should be investigated for the specific purpose of abdominal imaging.

Radiofrequency phase maps that can be retrieved from Eq. (3) can potentially be used for electric properties tomography.[51] We did not focus on it in this study, but provided the examples of RF phase maps in human brain (Figure 7).

5 | CONCLUSIONS

In this work we show the importance of the proper choice of sequence parameter settings, such as TR, FA, and number of RF phase increment steps to achieve a high accuracy and precision in quantitative parameter estimation using the PLANET method at realistic SNR levels. Interestingly, this combination holds over a wide range of relaxation times and does not require an exact prior knowledge of T_1 and T_2 of the tissue. However, the PLANET model assumes a single-peak frequency distribution, which is not the case for some biological tissues, like human brain WM tissue, fat tissues, or bone marrow. The presence of two or more components influences the performance of the method and leads to systematic errors in the parameter estimates, which depend on the choice of FA and TR.

Using a high acquisition matrix in combination with a suitable method for removal of Gibbs ringing artifacts improves the precision and accuracy of the parameter estimates, when PLANET is applied to a phantom with sharp signal intensity edges. For in vivo use, a relatively high acquisition matrix should be enough to minimize Gibbs ringing artifacts.

This evaluation of the accuracy and precision of PLANET should guide researchers who want to apply the method for different applications.

ORCID

Yulia Shcherbakova http://orcid.org/0000-0003-3521-1767

REFERENCES

1. Cheng HL, Stikov N, Ghugre NR, Wright GA. Practical medical applications of quantitative MR relaxometry. *J Magn Reson Imaging*. 2012;36:805–824.
2. Riederer SJ, Lee JN, Farzaneh F, Wang HZ, Wright RC. Magnetic resonance image synthesis. *Clinical implementation. Acta Radiol*. 1986;369:466–468.
3. Blystad I, Warntjes J, Smedby O, Landtblom A-M, Lundberg P, Larsson E-M. Synthetic MRI of the brain in a clinical setting. *Acta Radiol*. 2012;53:1158–1163.
4. Ma D, Gulani V, Seiberlich N, et al. Magnetic resonance fingerprinting. *Nature*. 2013;495:187–192.
5. Bernstein M, King KE, Zhou XJ, Fong W, Handbook of MRI Pulse Sequences. Cambridge, MA: Academic Press; 2005.
6. Look DC, Locker DR. Time saving in measurement of NMR and EPR relaxation times. *Rev Sci Instrum*. 1970;41:250–251.
7. Homer J, Beevers MS. Driven-equilibrium single-pulse observation of T1 relaxation. A reevaluation of a rapid "new" method for determining NMR spin-lattice relaxation times. *J Magn Reson*. 1985;63:287–297.
8. Deoni S, Rutt BK, Peters TM. Rapid combined T1 and T2 mapping using gradient recalled acquisition in the steady state. *Magn Reson Med*. 2003;49:515–526.
9. Deoni S. High-resolution T1 mapping of the brain at 3T with driven equilibrium single pulse observation of T1 with high-speed incorporation of RF field inhomogeneities (DESPOT1-HIFI). *J Magn Reson Imaging*. 2007;26:1106–1111.
10. Welsch GH, Scheffler K, Mamisch TC, et al. Rapid estimation of cartilage T2 based on double echo at steady state (DESS) with 3 Tesla. *Magn Reson Med*. 2009;62:544–549.
11. Heule R, Ganter C, Bieri O. Triple echo steady-state (TESS) relaxometry. *Magn Reson Med*. 2014;71:230–237.
12. Scheffler K, Hennig J. T1 quantification with inversion recovery TrueFISP. *Magn Reson Med*. 2001;45:720–723.
13. Deoni S, Ward HA, Peters TM, Rutt BK. Rapid T2 estimation with phase-cycled variable nutation steady-state free precession. *Magn Reson Med*. 2004;52:435–439.
14. Deoni S. Transverse relaxation time (T2) mapping in the brain with off-resonance correction using phase-cycled steady-state free precession imaging. *J Magn Reson Imaging*. 2009;30:411–417.
15. Schmitt P, Griswold MA, Jakob PM, et al. Inversion recovery TrueFISP: quantification of T(1), T(2), and spin density. *Magn Reson Med*. 2004;51:661–667.
16. Nguyen D, Bieri O. Motion-insensitive rapid configuration relaxometry. *Magn Reson Med*. 2017;78:518–526.
17. Shcherbakova Y, van den Berg C, Moonen C, Bartels LW. PLANET: an ellipse fitting approach for simultaneous T1 and T2 mapping using phase-cycled balanced steady-state free precession. *Magn Reson Med*. 2018;79:711–722.
18. Miller KL. Asymmetries of the balanced SSFP profile. I: Theory and observation. *Magn Reson Med*. 2010;63:385–395.
19. Miller KL, Smith SM, Jezzard P. Asymmetries of the balanced SSFP profile. II: White matter. *Magn Reson Med*. 2010;63:396–406.
20. Does MD, Beaulieu C, Allen PS, Snyder RE. Multi-component T1 relaxation and magnetisation transfer in peripheral nerve. *Magn Reson Imaging*. 1998;16:1033–1041.
21. Laule C, Vavasour IM, Moore G, et al. Water content and myelin water fraction in multiple sclerosis. A T2 relaxation study. *J Neurol*. 2004;251:284–293.
22. Stanisz GJ, Odrobina EE, Pun J, et al. T1, T2 relaxation and magnetization transfer in tissue at 3T. *Magn Reson Med*. 2005;54:507–512.
23. Oh J, Han ET, Pelletier D, Nelson, . SJ. Measurement of in vivo multi-component T2 relaxation times for brain tissue using multi-slice T2 prep at 1.5 and 3 T. *Magn Reson Imaging*. 2006;24:33–43.
24. Laule C, Vavasour IM, Kolind SH, et al. Magnetic resonance imaging of myelin. *Neurotherapeutics*. 2007;4:460–484.
25. Deoni S, Rutt BK, Arun T, Pierpaoli C, Jones DK. Gleaning multicomponent T1 and T2 information from steady-state imaging data. *Magn Reson Med*. 2008;60:1372–1387.

26. Kolind SH, Mädler B, Fischer S, Li D, MacKay AL. Myelin water imaging: implementation and development at 3.0T and comparison to 1.5T measurements. *Magn Reson Med*. 2009;62:106–115.
27. Prasloski T, Rauscher A, MacKay AL, et al. Rapid whole cerebrum myelin water imaging using a 3D GRASE sequence. *NeuroImage*. 2012;63:533–539.
28. Labadie C, Lee JH, Rooney WD, et al. Myelin water mapping by spatially regularized longitudinal relaxographic imaging at high magnetic fields. *Magn Reson Med*. 2014;71:375–387.
29. Zhang J, Kolind SH, Laule C, Mackay AL. Comparison of myelin water fraction from multiecho T2 decay curve and steady-state methods. *Magn Reson Med*. 2015;73:223–232.
30. Bouhrara M, Spencer RG. Improved determination of the myelin water fraction in human brain using magnetic resonance imaging through Bayesian analysis of mcDESPOT. *NeuroImage*. 2016;127:456–471.
31. Rioux JA, Levesque IR, Rutt BK. Biexponential longitudinal relaxation in white matter: characterization and impact on T1 mapping with IR-FSE and MP2RAGE. *Magn Reson Med*. 2016;75:2265–2277.
32. Bouhrara M, Spencer RG. Rapid simultaneous high-resolution mapping of myelin water fraction and relaxation times in human brain using BMC-mcDESPOT. *NeuroImage*. 2017;147:800–811.
33. Alonso-Ortiz E, Levesque IR, Pike GB. MRI-based myelin water imaging: a technical review. *Magn Reson Med*. 2015;73:70–81.
34. Xiang QS, Hoff MN. Banding artifact removal for bSSFP imaging with an elliptical signal model. *Magn Reson Med*. 2014;71:927–933.
35. Louis LM, Frayne R. Analytical characterization of RF phase-cycled balanced steady-state free precession. *Concept Magn Reson Part A*. 2009;34A:133–143.
36. Wansapura JP, Holland SK, Dunn RS, Ball WS. NMR relaxation times in the human brain at 3.0 Tesla. *J Magn Reson Imaging*. 1999;9:531–538.
37. Björk M, Ingle RR, Gudmundson E, Stoica P, Nishimura DG, Barral JK. Parameter estimation approach to banding artifact reduction in balanced steady-state free precession. *Magn Reson Med*. 2014;72:880–892.
38. Yarnykh VL. Actual flip-angle imaging in the pulsed steady state: a method for rapid three-dimensional mapping of the transmitted radiofrequency field. *Magn Reson Med*. 2007;57:192–200.
39. Sijbers J, Den Dekker AJ, Van Audekerke J, Verhoye M, Van Dyck D. Estimation of the noise in magnitude MR images. *Magn Reson Imaging*. 1998;16:87–90.
40. Firbank MJ, Coulthard A, Harrison RM, Williams ED. A comparison of two methods for measuring the signal to noise ratio on MR images. *Phys Med Biol*. 1999;44:N261–N264.
41. Kroeker RM, Mark HR. Analysis of biological NMR relaxation data with continuous distributions of relaxation times. *J Magn Reson*. 1986;69:218–235.
42. Preibisch C, Deichmann R. Influence of RF spoiling on the stability and accuracy of T1 mapping based on spoiled FLASH with varying flip angles. *Magn Reson Med*. 2009;61:125–135.
43. Whittall KP, Mackay AL, Graeb DA, Nugent RA, Li D, Paty DW. In vivo measurement of T2 distributions and water contents in normal human brain. *Magn Reson Med*. 1997;37:34–43.
44. Stanisz GJ, Kecojevic A, Bronskill MJ, Henkelman RM. Characterizing white matter with magnetization transfer and T2. *Magn Reson Med*. 1999;42:1128–1136.
45. Bieri O, Scheffler K. Optimized balanced steady-state free precession magnetization transfer imaging. *Magn Reson Med*. 2007;58:511–518.
46. Aubert-Broche B, Evans AC, Collins L. A new improved version of the realistic digital brain phantom. *NeuroImage*. 2006;32:138–145.
47. Kellner E, Dhital B, Kiselev VG, Reisert M. Gibbs-ringing artifact removal based on local subvoxel-shifts. *Magn Reson Med*. 2016;76:1574–1581.
48. Bieri O, Markl M, Scheffler K. Analysis and compensation of eddy currents in balanced SSFP. *Magn Reson Med*. 2005;54:129–137.
49. Bojorquez JZ, Bricq S, Acquitter C, Brunotte F, Walker PM, Lalande A. What are normal relaxation times of tissues at 3T? *Magn Reson Imaging*. 2017;35:69–80.
50. Hal R, Flusser J. Numerically stable direct least squares fitting of ellipses. In: Proceedings of the 6th International Conference in Central Europe on Computer Graphics, Visualization and Computer Vision ed V Skala, Plzen, Czech Republic. 1998;1:125–132.
51. Katscher U, van den Berg C. Electric properties tomography: biochemical, physical and technical background, evaluation and clinical applications. *NMR Biomed*. 2017;30:e3729.

SUPPORTING INFORMATION

Additional supporting information may be found online in the Supporting Information section at the end of the article.

FIGURE S1 Simulation results at low SNR levels for a single-component WM model at 3T (T_1 = 830 ms, T_2 = 80 ms) and Δf_0 = 10 Hz. A, Signal-to-noise ratio as a function of FA and TR. B, Relative errors ε (in percent) of the parameter estimates compared with their true values. C, Standard deviation STD (in percent) of the parameter estimates compared with their mean values (the white line corresponds to FA = FA_E, only the region to the right is allowed). D, Distribution of the parameter estimates in the boxplots as a function of number of RF phase increment steps **N** (black dashed lines correspond to the true parameter values)

FIGURE S2 Noise-free simulation results for a two-component WM model. The relative errors ε (in percent) of the parameter estimates compared with their true values (of the dominant component) for the different cases. A, Dominant component (D) has T_{1L} = 1000 ms and T_{2L} = 80 ms, volume fraction of 0.88; myelin component (M) has T_{1s} = 400 ms and T_{2s} = 20 ms, volume fraction of 0.12, shift Δf = 20 Hz. B, Dominant component (D) has T_{1L} = 1000 ms and T_{2L} = 80 ms, volume fraction of 0.88; myelin component (M) has T_{1s} = 1000 ms and T_{2s} = 80 ms, volume fraction of 0.12, shift Δf = 20 Hz. C, Dominant component (D) has T_{1L} = 1000 ms

and T_{2L} = 80 ms, volume fraction of 0.88; myelin component (M) has T_{1s} = 400 ms and T_{2s} = 20 ms, volume fraction of 0.12, shift Δf = 0 Hz. D, Dominant component (D) has T_{1L} = 1000 ms and T_{2L} = 80 ms, volume fraction of 0.5; myelin component (M) has T_{1s} = 400 ms and T_{2s} = 20 ms, volume fraction of 0.5, shift Δf = 0 Hz. E, Dominant component (D) has T_{1L} = 1000 ms and T_{2L} = 80 ms, volume fraction of 0.5; myelin component (M) has T_{1s} = 400 ms and T_{2s} = 20 ms, volume fraction of 0.5, shift Δf = 20 Hz. Note that the color bars are scaled differently

FIGURE S3 Experimental results from the phantom study: T_1 map calculated using the PLANET method at high SNR level, additionally acquired B_1 map for correction, and T_1 map corrected using the B_1 map

FIGURE S4 Additional results of simulations on a numerical brain phantom. A, Distribution of T_1 estimates in histograms and boxplots for WM for different reconstructions of simulated *k*-space. The blue bars correspond to the results without Gibbs ringing correction, and the orange bars correspond to the results after the Gibbs ringing correction applied. The red line is the true parameter value. B, Distribution of T_2 estimates in histograms and boxplots for WM for different reconstruction of simulated *k*-space. The blue bars correspond to the results without Gibbs ringing correction, and the orange bars correspond to the results after Gibbs ringing correction is applied. The red line is the true parameter value

TABLE S1 Optimal parameter settings and minimum required SNR for different relaxation time combinations for a single-component signal model

How to cite this article: Shcherbakova Y, van den Berg CAT, Moonen CTW, Bartels LW. On the accuracy and precision of PLANET for multiparametric MRI using phase-cycled bSSFP imaging. *Magn Reson Med*. 2019;81:1534–1552. https://doi.org/10.1002/mrm.27491